EMBRY-RIDDLE
Aeronautical University™
SCHOLARLY COMMONS

Publications

9-8-2017

Ionospheric Gravity Waves Driven by Oceanic Gravity Waves in Resonance: A Modeling Study in Search of Their Spectra

Michael P. Hickey
Embry-Riddle Aeronautical University, hicke0b5@erau.edu

Yonghui Yu
Nanjing University of Aeronautics and Astronautics, yuyong@nuaa.edu.cn

Follow this and additional works at: https://commons.erau.edu/publication

Part of the Atmospheric Sciences Commons

Ionospheric Gravity Waves Driven by Oceanic Gravity Waves in Resonance: A Modeling Study in Search of Their Spectra

Yonghui Yu[1] (iD) **and Michael P. Hickey[2]** (iD)

[1]College of Astronautics, Nanjing University of Aeronautics and Astronautics, Nanjing, China, [2]Department of Physical Sciences and Center for Space and Atmospheric Research, Embry-Riddle Aeronautical University, Daytona Beach, FL, USA

Abstract Ionospheric observations associated with the 2011 Tohoku tsunami have revealed gravity waves having spectral characteristics that depend on their proximity to the epicenter. There is a preponderance of medium-scale waves in the vicinity of the epicenter, a significant bifurcation into short- and long-period waves over the Hawaiian archipelago, and a narrow and rich spectrum of waves over the West Coast and inland of the United States (U.S.). Guided by these previous observations, we consider wave sources as triads of nonlinearly interacting oceanic gravity waves, whose wave parameters satisfy resonant conditions. These waves are simulated using a 2-D nonlinear model describing gravity wave propagation in order to explain the observations of tsunamigenic traveling ionospheric disturbances (TIDs) associated with the Tohoku event.

1. Introduction

The Tohoku tsunami on 11 March 2011 was excited by a submarine earthquake in the Pacific Ocean around midlatitudes (38.322°N, 142.369°E) and at about 05 h 46 m universal time (UT). Various measurement techniques are used to detect traveling ionospheric disturbances (e.g., Komjathy et al., 2012; Liu et al., 2011; Occhipinti et al., 2013), which are subsequently generated by the coupling between Earth's ocean and ionosphere via atmospheric gravity waves (AGWs). One frequently used measurement technique is by the monitoring of total electron content (TEC) in the ionosphere with the Global Positioning System (GPS) array (e.g., Azeem et al., 2017; Crowley et al., 2016; Galvan et al., 2012; Rolland et al., 2011), while another technique that relies on clear observing conditions is by imaging the airglow modulation in the upper atmosphere (Makela et al., 2011; Smith et al., 2015).

In the past, Hickey et al. (2009) used a spectral full-wave model to study tsunami-driven gravity waves and their effects on the ionosphere. Their predicted effects on mesospheric and thermospheric airglow emissions were studied by Hickey, Schubert et al. (2010), and the nonlinear interactions of these waves with the mean state were also examined by Hickey, Walterscheid et al. (2010). Vadas et al. (2015) used a 3-D model to excite AGWs by an ocean surface wave packet, and their findings were used to explain the observation by Makela et al. (2011), in which some AGWs in the airglow layer were seen 1 h before the Tohoku tsunami reached Hawaii. The observation of Galvan et al. (2012) was explained by Yu et al. (2015, 2017) using a 2-D, time-dependent, and nonlinear model (Yu et al., 2009) including ion chemistry and dynamics.

Long oceanic gravity waves (tsunami) propagate along the sea surface with the shallow-water wave speed ($\sqrt{gh}$) largely dependent on gravity (g) and depth of the ocean (h) (Holton, 2012). In the 2011 Tohoku epicentral region, Rolland et al. (2011) first imaged with a GPS-derived TEC technique concentric gravity waves emerging outward with a speed of 225 ± 10 ms^{-1} and a frequency of 1.8 ± 0.2 mHz. The Deep-ocean Assessment and Reporting of Tsunamis (DART) measured a dominant wave period of 32 min and an average wave speed of 243 ms^{-1} southeastward between the epicenter and the ocean buoy no. 21419 (Galvan et al., 2012), and the derived horizontal wavelength was about 466.6 km.

Crowley et al. (2016) detected TIDs associated with the tsunami over the West Coast of the United States about 10 h after the earthquake and at an azimuth of N105.2°E. They found a waveform with a period of about 15.1 min, a horizontal wavelength of about 194.8 km, and a horizontal phase speed of about 233.0 ms^{-1}. These measurements are compatible with the short-period waves (14.2 ± 2.7 min, 189.9 ± 4.9 km, and 222.9 ± 52.4 ms^{-1}), which were observed in an airglow response by Makela et al. (2011) over Hawaii about 5 h after the earthquake. Makela et al. (2011) also showed another longwave feature (26.2 ± 3.1 min, 290.0 ± 12.5 km, and 184.5 ± 33.8 ms^{-1}). Over the west inland region of the U.S., Azeem et al.

(2017) observed rich spectra of TIDs with periods between 14 and 30 min, horizontal wavelengths between 150 and 400 km, and horizontal phase speeds between 180 and 260 ms^{-1}. Reverse ray tracing showed that the Tohoku tsunami was the likely source of the TIDs.

A wide range of wave periods (ranging from about 8.3 to 32.0 min) and horizontal wavelengths (about 107.5 to 466.6 km) are seen in observations, both in the near field (Galvan et al., 2012; Rolland et al., 2011) and in the far fields (Azeem et al., 2017; Crowley et al., 2016; Makela et al., 2011), while observed horizontal phase speeds (about 150.7 to 275.3 ms^{-1}) are more consistent. The purpose of this paper is to reconcile these seemingly disparate wave parameters by invoking the resonant theory of oceanic wave interaction in our study. We hypothesize that waves observed in the far fields (described above) may result from resonant interactions of some primary oceanic gravity waves in the near field (described above). We first plan to briefly describe the resonant theory of wave interaction in the ocean in section 2, which subsequently includes an introduction to our 2-D modeling of tsunamigenic gravity waves in the ionosphere (Yu et al., 2017). Second, we present results of source spectra and corresponding ionospheric simulations in section 3. We finally provide a discussion and conclusions in sections 4 and 5, respectively.

2. Theory and Modeling

Phillips (1960) first proposed a theory of the nonlinear interaction between pairs of gravity waves on the water surface. In particular, the amplitude of secondary waves became bounded in time and large under the shallow-water condition. Longuet-Higgins (1962) further calculated the coupling magnitude of two interacting waves and estimated the modification in the ocean wave spectrum. McComas and Bretherton (1977) numerically computed spectral energy transfer among oceanic waves of nonlinearly interacting triads, whose wave numbers (k_1, k_2, k_3) and frequencies $(\omega_1, \omega_2, \omega_3)$ satisfy resonant conditions $(k_3 = k_1 \pm k_2, \omega_3 = \omega_1 \pm \omega_2)$.

A 2-D, nonlinear, and time-dependent model of atmospheric gravity wave propagation (Yu et al., 2009, 2015) that incorporates ion chemistry and dynamics (Yu et al., 2017) is used in the current study. The Navier-Stokes equations are solved in the model with an explicit Lax-Wendroff and an implicit Newton-Raphson scheme for wave propagation in a nonisothermal and viscous atmosphere in the presence of background winds (Yu et al., 2009). Rayleigh friction and Newtonian cooling serve as a sponge layer near the upper boundary of the model (Walterscheid & Schubert, 1990), while lateral boundaries are periodic over an integer number of horizontal wavelengths to simulate a horizontally infinite domain. A complete description of the model equations is beyond the scope of our present study but can be found in the works of Yu et al. (2009).

The applied ion dynamics solves the hydromagnetic momentum equation, the ion continuity equation, and the equation for charge neutrality. The applied ion chemistry solves the fluctuations of the number densities of all major ions (O^+, N_2^+, O_2^+, and NO^+) and then calculates the vertical TEC (VTEC) by integrating over altitude the electron number density (n_e), which is coupled by charge neutrality with the sum of the number densities of all major ions (described above) (Hickey et al., 2009; Yu et al., 2017). A complete description of the ion chemistry and dynamics is provided in the previous works of ion simulation by Hickey et al. (2009) and Yu et al. (2017).

The Mass Spectrometer and Incoherent Scatter-90 model (Hedin, 1991) is used to describe the ambient neutral atmosphere for the 11 March 2011 Tohoku tsunami. The horizontal mean winds are incorporated using the Horizontal Wind Model-93 (Hedin et al., 1996) using the same input parameters. We apply moderately high solar and geomagnetic conditions (Komjathy et al., 2012) for the event ($A_p = 37$; $F_{10.7} = 121.5$ and its 81 day mean is 104.4) (ftp://ftp.ngdc.noaa.gov/STP/GEOMAGNETIC_DATA/INDICES/KP_AP/). Three geographic cases of interest are as follows: (1) the epicenter (38.322°N, 142.369°E) and 05 h 46 m (UT) (Galvan et al., 2012; Rolland et al., 2011); (2) the Big Island of Hawaii (19.6°N, 203.5°E) and 13 h 07 m (UT) according to DART buoy no. 51407 (Makela et al., 2011); and (3) the west coast of California (39.328°N and 127.013°W) and 15 h 00 m (UT) according to the bottom pressure recorded (BPR) data by a local DART buoy (Azeem et al., 2017).

On the lower boundary of the 2-D model (sea level) we implement one or three ocean surface waves forced by prescribing three time-dependent vertical displacements ξ_1, ξ_2, and ξ_3 (Yu et al., 2015, 2017).

Table 1
Wave Parameters of a Triad

	Horizontal wave number	Extrinsic wave frequency	Vertical wave number
Primary wave	$k_1 = 2\pi/\lambda_h{}^1$ $= 2\pi/(584.46 \text{ km})$ $= 1.075 \times 10^{-5} \text{m}^{-1}$	$\omega_1 = 2\pi/\tau_1$ $= 2\pi/(45.18 \text{ min})$ $= 2.318 \times 10^{-3} \text{s}^{-1}$	$m_1 = 2\pi/\lambda_z{}^1$ $= 2\pi/(146.73 \text{ km})$ $= 4.282 \times 10^{-5} \text{m}^{-1}$
Secondary wave	$k_2 = 2\pi/\lambda_h{}^2$ $= 2\pi/(292.23 \text{ km})$ $= 2.150 \times 10^{-5} \text{m}^{-1}$	$\omega_2 = 2\pi/\tau_2$ $= 2\pi/(22.59 \text{ min})$ $= 4.636 \times 10^{-3} \text{s}^{-1}$	$m_2 = 2\pi/\lambda_z{}^2$ $= 2\pi/(162.86 \text{ km})$ $= 3.858 \times 10^{-5} \text{m}^{-1}$
Tertiary wave	$k_3 = 2\pi/\lambda_h{}^3$ $= 2\pi/(194.82 \text{ km})$ $= 3.225 \times 10^{-5} \text{m}^{-1}$	$\omega_3 = 2\pi/\tau_3$ $= 2\pi/(15.06 \text{ min})$ $= 6.954 \times 10^{-3} \text{s}^{-1}$	$m_3 = 2\pi/\lambda_z{}^3$ $= 2\pi/(208.19 \text{ km})$ $= 3.018 \times 10^{-5} \text{m}^{-1}$

These are described analytically as one or three traveling sinusoidal waves modulated by their Gaussian envelops over time:

$$\xi_1(x,0,t) = A_m \exp\left[-(t-\tau_{c1})^2/2\Delta t_1{}^2\right] \sin(k_1 x - \omega_1 t); \tag{1}$$

$$\xi_2(x,0,t) = \left(A_m/\sqrt{3}\right) \sum_{j=1}^{3} \exp\left[-(t-\tau_{c2})^2/2\Delta t^2{}_j\right] \sin\left(k_j x - \omega_j t\right); \tag{2}$$

$$\xi_3(x,0,t) = \left(A_m/\sqrt{6}\right) \sum_{j=1}^{2} \exp\left[-(t-\tau_{c3})^2/2\Delta t^2{}_j\right] \sin\left(k_j x - \omega_j t\right)$$
$$+ \left(A_m/\sqrt{3}\right) \exp\left[-(t-\tau_{c3})^2/2\Delta t_3{}^2\right] \sin(k_3 x - \omega_3 t). \tag{3}$$

Here ξ_1, ξ_2, and ξ_3 are applied to cases 1, 2, and 3, respectively, as defined previously. Also, x is the horizontal position and t is time. The remaining parameters are the maximum displacement of the ocean surface ($A_m = 0.76$ m) (Galvan et al., 2012; Yu et al., 2015, 2017); the center time (τ_{c1}: 05 h 46 m, τ_{c2}: 13 h 07 m, τ_{c3}: 15 h 00 m) (Azeem et al., 2017; Crowley et al., 2016; Galvan et al., 2012; Makela et al., 2011; Rolland et al., 2011); the Gaussian packet width ($\Delta t_j = \tau_j/2$ before τ_{c1}, τ_{c2}, or τ_{c3}, and $\Delta t_j = \tau_j$ after τ_{c1}, τ_{c2}, or τ_{c3}) (Yu et al., 2015, 2017); the horizontal wave number ($k_j = 2\pi/\lambda_h{}^j$); and the extrinsic wave frequency ($\omega_j = 2\pi/\tau_j$). Also, τ_j is the extrinsic wave period, $\lambda_H{}^j$ is the horizontal wavelength, and the j subscript or j superscript values of 1, 2, and 3 indicate the primary, secondary, and tertiary waves, respectively (Table 1).

We use an approximate form of the dispersion relation (Gossard & Hooke, 1975) to calculate the vertical wave numbers (m_j) (Table 1) at 250 km altitude where the Brunt-Väisälä period is about 11 min (Yu et al., 2015). In equation (4), $\lambda_z{}^j$ is the vertical wavelength, N is the nonisothermal Brunt-Väisälä frequency, and other symbols are as previously defined:

$$m_j{}^2 = \left(\frac{2\pi}{\lambda_z^j}\right)^2 = \left(\frac{N^2}{\omega_j{}^2} - 1\right) k_j{}^2. \tag{4}$$

We use a primary wave with a period of about 45.18 min (Table 1) propagating toward the southeast of the epicenter. A configured spectrum of wave triads (equation (3)) based on this tends to agree with the spectrogram of the BPR data by a local DART buoy near the west coast of California (described later in detail) (Azeem et al., 2017). The secondary wave results from a resonant interaction of a pair of the primary waves ($k_2 = k_1 + k_1$, $\omega_2 = \omega_1 + \omega_1$). The tertiary wave results from a resonant interaction of a pair of the primary and secondary waves ($k_3 = k_1 + k_2$, $\omega_3 = \omega_1 + \omega_2$) (Table 1). During the surface propagation of the oceanic gravity waves, we assume that an energy transfer takes place from the primary wave to the secondary wave and further to the tertiary wave in a matter of a few hours (Azeem et al., 2017; Crowley et al., 2016; Makela et al., 2011). The secondary and tertiary waves may therefore grow in time and become comparable with the primary wave (in amplitude) within several hours (Longuet-Higgins, 1962; Phillips, 1960). In so doing, we presume an equal combination of the primary, secondary, and tertiary waves in equation (2). A further reduced amplitude is reasonably prescribed to the primary and secondary waves in equation (3).
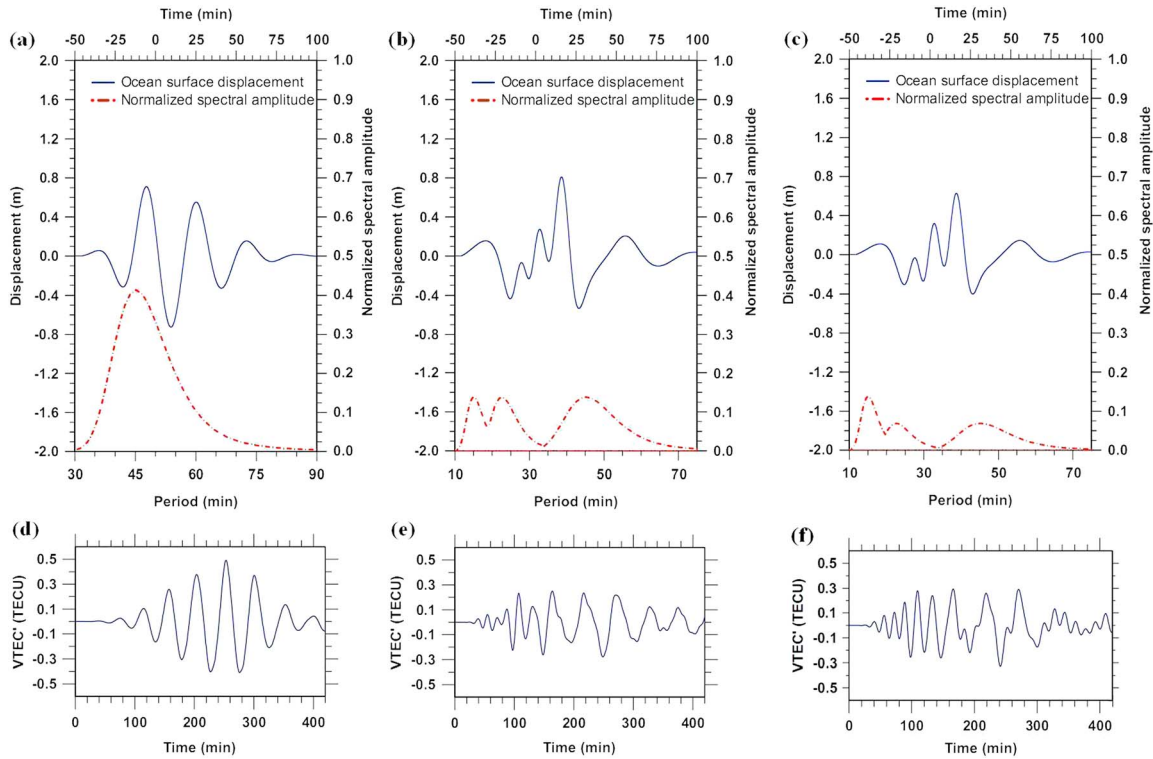
Figure 1. (a–c) Ocean surface displacement (solid line, upper x axis, left y axis) and normalized spectral amplitude (dashed dotted line, lower x axis, right y axis) and (d–f) corresponding time series of the VTEC fluctuations at an arbitrary horizontal position of 188 km (due to periodic lateral boundary condition) from the start driven by an ocean surface wave ξ_1 (Figures 1a and 1d), ξ_2 (Figures 1b and 1e), and ξ_3 (Figures 1c and 1f).

Equation (2) describes an intermediate state between the states described by (1) and (3). In this paper, the resonant oceanic gravity waves are modeled in some detail: The phase velocities of the source waves have a value of about 215.6 ms^{-1} (Table 1), a value which was commonly observed in the near and far fields by Azeem et al. (2017), Crowley et al. (2016), Makela et al. (2011), and Rolland et al. (2011) and which also lies within a likely range reported by Galvan et al. (2012). Our motivation is to explain the fairly complex sets of observations by a single basic theory.

3. Results

The time variations of the ocean surface displacements ξ_1, ξ_2, and ξ_3 are shown in Figures 1a–1c, respectively. Note that displacements are plotted with respect to their center time (as previously defined). They occur at negative time values before their center time. We calculate the spectral amplitude for the spectrum of waves by applying the fast Fourier transform to these time series of ξ_1, ξ_2, and ξ_3 and then normalize them for each wave component by partitioning a fraction of the total power amplitude. The primary wave (ξ_1) at the epicenter is derived with a maximum normalized spectral amplitude (MNSA) of about 0.42 at 45.18 min (τ_1), a full width at half maximum (FWHM) of about 19.77 min, a continuum spectrum of periods ranging from 30 to 90 min, and a duration of 150 min (Figure 1a). The spectral characteristics corresponding to two triads of the primary, secondary, and tertiary waves (ξ_2 and ξ_3) are also shown in Figures 1b and 1c, respectively. ξ_2 is derived with a MNSA of about 0.14 at 45.18 min (τ_1), 22.59 min (τ_2), and 15.06 min (τ_3), respectively (Figure 1b). ξ_3 is derived with a MNSA of about 0.07 at 45.18 min (τ_1) and 22.59 min (τ_2), respectively, and a MNSA of about 0.14 at 15.06 min (τ_3) (Figure 1c). ξ_2 and ξ_3 are both derived with a continuum spectrum of periods ranging from 10 to 74 min and a duration of 150 min (Figures 1b and 1c). These ocean surface waves ξ_1, ξ_2, and ξ_3 start at their corresponding locations and times and propagate toward the N135.00°E (Yu et al., 2017), N134.00°E (Makela et al., 2011), and N105.16°E directions (Crowley et al., 2016), respectively.
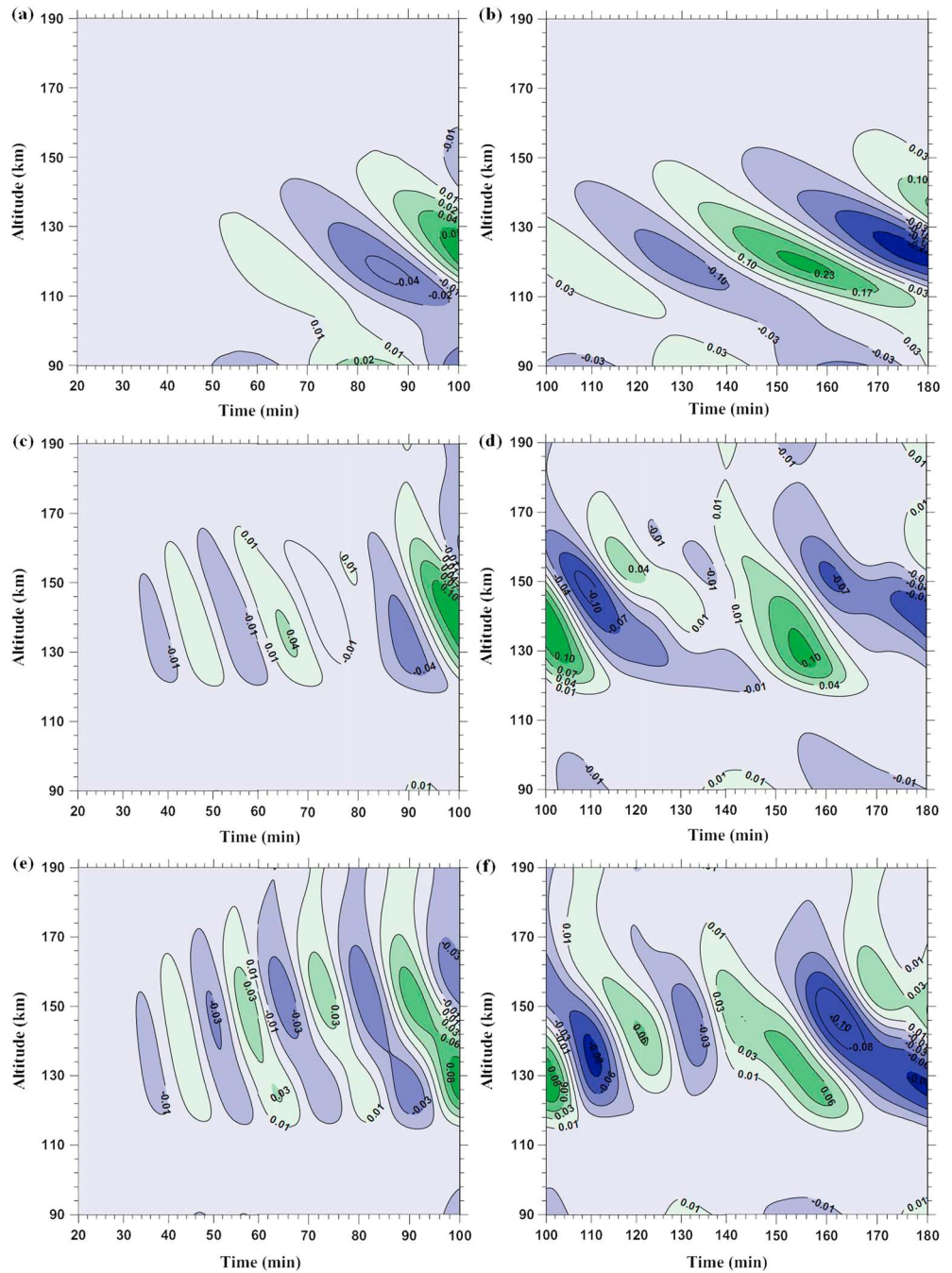
Figure 2. Relative variations of the electron number density due to ionospheric gravity waves originating from an ocean surface wave (a and b) ξ_1, (c and d) ξ_2, and (e and f) ξ_3. Note that contour colors vary from panel to panel and are only intended to help distinguish positive and negative variations.

The VTEC fluctuations associated with ξ_1, ξ_2, and ξ_3 are shown in Figures 1d–1f, respectively, which are calculated by integrating the electron number density (n_e) over height at an arbitrary horizontal position of 188 km (due to periodic lateral boundary condition) and at each time following the tsunami onset or arrival (as previously described). The mean electron number density ($\overline{n_e}$) is modeled as a Chapman layer (Hickey et al., 2009; Yu et al., 2017) with the F_2 peak (250 km) (Crowley et al., 2016) and an E layer peak (105 km) for a condition of moderately high solar activity. The mean TEC values corresponding to cases 1, 2, and 3 are 20.1, 18.1, and 18.7 TECU, respectively, where 1 TECU = 10^{16} el m^{-2}.

Figure 1d shows a well-formed wave packet embodying information about the period of the primary wave from the epicenter (Figure 1a). The wave packet grows in amplitude from about 60 min, reaches a maximum value of about 0.5 TECU at 250 min, and then decreases to a small value by about 420 min. Figure 1e shows a more complicated wave structure combining information about the primary, secondary, and tertiary waves (Figure 1b) originating from the Big Island of Hawaii. At times earlier than 100 min, the wave structure mainly exhibits variations having period signatures of the tertiary and secondary waves, while after a time of 100 min variations due to the secondary and primary waves dominate. Figure 1f shows a similarly complicated wave structure exhibiting variations having signatures of the primary, secondary, and tertiary waves (Figure 1c) and originating from the west coast of California. This wave structure conspicuously carries period signatures of the tertiary and secondary waves before about 140 min and the primary wave from about 140 to 300 min; after 300 min the wave amplitude becomes significantly reduced.

We now examine the vertical structure of the electron density variations. Figure 2 shows the relative variations of the electron number density ($(n_e^a - \overline{n_e})/\overline{n_e}$, where n_e^a is an averaged electron number density over the horizontal wavelength of the primary wave) as a function of altitude and time. The times shown are with respect to the time of the tsunami onset or the arrival time (as previously described).

We find that the fluctuations driven by the tertiary wave first achieve a noticeable amplitude (0.01) of the electron density variation at about 35 min and 150 km (Figure 2c), approximately 30 min before those driven by the primary wave (at about 65 min and 140 km, Figure 2a). The fluctuations driven by the tertiary wave would therefore provide the earliest sign of a TID (assuming that differences in atmospheric conditions between the epicenter and Big Island of Hawaii were not significant at those times). This is clearly evident in the VTEC results shown earlier (compare Figures 1d and 1e).

There are two fundamental and effective ways to identify the fluctuations respectively driven by the secondary and tertiary waves. First, the fluctuations driven by the tertiary wave propagate upward faster than those driven by the secondary wave and appear at an earlier time and a higher altitude. Second, the fluctuations driven by the tertiary (about 15 min) and secondary waves (more than 20 min) have significantly different periods, by which they can be easily distinguished.

In Figure 2c, the fluctuations driven by the tertiary wave dominate till about 60 min and coexist with those due to the secondary wave between about 60 and 100 min. The fluctuations driven by the secondary wave dominate between about 100 and 140 min and those due to the primary wave dominate at later times (Figure 2d). In Figure 2e, the fluctuations driven by the tertiary and secondary waves strongly interfere leading to reinforcement or cancelation between about 60 and 100 min, while those due to the primary wave dominate at times later than 140 min (Figure 2f). Reinforcement or cancelation of waves can be identified by superposition of two waves at the same time, one with a higher altitude and another lower. Interference effects can be seen in the results presented for ξ_2 and ξ_3.

In case 1 the fluctuations driven by the primary wave achieve largest amplitude at about 250 min and diminish gradually due to atmospheric viscosity at later times (Figure 1d). In case 3 most conspicuous wave feature occurs about 300 min later, when superposition of smaller-scale waves leads to much reduced observable amplitude (Figure 1f) due to cancelation in the vertical (not shown).

4. Discussion

Galvan et al. (2012) and Rolland et al. (2011) reported most visible wave activity toward the northwest of the epicenter, but Yu et al. (2017) used a model to reason that long-range wave propagation would occur for propagation toward the southeast. Our simulations presented here indicate that resonant wave components with shorter period and larger vertical wavelength (Table 1) dominate at earlier times and higher altitudes, while longer-period components with shorter vertical wavelength should dominate at later propagation times (Figures 2c–2f). We have shown that ionospheric gravity wave is capable of interference; superposition of ionospheric gravity waves can lead either to reinforcement or cancelation (e.g., Figure 2e).

We find that the first sign due to the tertiary wave in the ionosphere (150 km) precedes the first sign due to the primary wave (140 km) by about 30 min (compare Figures 2a and 2c). Makela et al. (2011) observed some "early" TIDs in the 630 nm airglow layer (peak at 250 km) an hour before the Tohoku tsunami reached Hawaii. Our simulations reveal that the fluctuations driven by the tertiary wave attain the lower F region ionosphere

half an hour sooner than those driven by the primary wave. Airglow observations of the 630 nm layer by Makela et al. (2011) involve a height integral of the airglow volume emission rate (brightness) over the entire emission layer. The results (not shown) of using a full-wave model show that the fluctuations driven by the secondary and tertiary waves will easily reach an altitude of 250 km, respectively. The fastest gravity wave fluctuations simulated and found at lower altitudes can be used to explain which part of the wave spectrum would contribute to the arrival of "early" gravity waves in the 630 nm layer.

The fluctuations driven by the tertiary and secondary waves shown between 20 and 140 min in the ionosphere (Figures 2c and 2d) are in general agreement by components with the short- and long-period TIDs described in the observations of Makela et al. (2011) in the 630 nm airglow layer, respectively. However, the fluctuations driven by the primary wave shown after 140 min in the ionosphere (Figure 2d) were absent in these observations. One possible explanation is that the vertical wavelength due to the primary wave at 250 km altitude is shorter than those due to the secondary (about 162.9 km) and tertiary waves (about 208.2 km), having a value of about 146.7 km (Table 1). The 630 nm airglow layer with a FWHM of about 50 km (Smith et al., 2015) may have a large vertical extent of about 100 km. Hence, a height integral of the airglow volume emission rate (brightness) over the emission layer may partially "smear" the gravity wave effects (cancelation). The 630 nm airglow layer tends to favor long vertical wavelength of waves (due to tertiary and secondary) while leading the shorter vertical wavelength of wave (due to primary) less favorable (e.g., Hickey & Yu, 2005).

A similar argument holds for the ability to observe TIDs based on TEC measurements. There was no trace of fluctuations due to the primary wave in the measurement reports by Azeem et al. (2017) and Crowley et al. (2016). Our simulations (Figures 1f and 2f) show that the fluctuations due to the primary wave exist about 140 min later. Azeem et al. (2017) proposed that a discernable TID requires the vertical wavelength of the underlying wave be much larger than the thickness of the *F* region ionospheric layer (about 100 km). This will ensure that in deriving the TEC, the electron density fluctuations survive the integration along the line of sight.

We have configured a triad of the primary, secondary, and tertiary oceanic waves near the West Coast of the U.S. (Figure 1c), whose spectrum is agreeable with the spectrogram of the BPR data by a local DART buoy (Azeem et al., 2017). The source spectrum presented in Figure 1c agrees well with the measurements: the sea surface waves had periods ranging from 10 to 70 min with most falling in the 10–30 min and 40–55 min bands (Azeem et al., 2017). In Figure 2e between 60 and 100 min, ionospheric gravity waves result from an interference of the fluctuations driven by resonant tertiary and secondary waves. They are coherent waves originating from the primary wave; the fluctuations driven by the secondary wave may be partially canceled by an interference with those due to the tertiary wave over the west inland region of the U.S. This effect of interference in the ionosphere may have already been observed by Crowley et al. (2016) in Shasta Lake, California (40.79°N, 122.19°W), between 17:00 and 19:00 UT: the amplitude and period of time series of TEC perturbations shown in their Figure 2a had respectively become reduced and longer since 18:00 UT.

5. Conclusions

We have formulated some primary oceanic waves with some period of about 45.18 min propagating toward the southeast of the epicenter. Because of the sparse population of GPS receivers in the southeast, ionospheric perturbations driven by ξ_1 could not be confirmed by the northwest observations of Galvan et al. (2012) and Rolland et al. (2011). We have also conjectured that secondary and tertiary oceanic gravity waves result from nonlinear resonant interactions of the primary tsunami waves accompanying their propagation along the ocean surface of the Pacific. Based on our hypothesis, we have configured a triad of the primary, secondary, and tertiary oceanic waves near the west coast of California. Their spectrum tends to agree well with the spectrogram of the BPR data by a local DART buoy (Azeem et al., 2017).

We used these waveforms to drive atmospheric gravity waves in our nonlinear, time-dependent model and to simulate the corresponding ionospheric perturbations, finding that ionospheric gravity waves driven by the secondary and tertiary waves coexist at early times in the TEC simulations. In particular, the fluctuations driven by the tertiary wave propagate faster vertically, attaining the lower *F* region ionosphere about 30 min sooner than those due to the primary wave. This may have already been

confirmed by the observations of Makela et al. (2011) over Hawaii, in which the simulated TEC response due to the tertiary and secondary waves tends to match by components the short- and long-period waves observed in the 630 nm airglow layer, respectively. Over the West Coast of the U.S. Crowley et al. (2016) have, in fact, observed the fluctuations in the ionosphere due to the tertiary wave, while over the west inland of the U.S. Azeem et al. (2017) have actually observed richer spectra of waves in the ionosphere which tend to agree with the fluctuations driven by the tertiary and secondary waves simulated here.

We have postulated that the source waves in resonance can explain several puzzling aspects of the TID observations associated with the 2011 Tohoku tsunami. Our simulations of the electron number density and TEC fluctuations seem to explain the far-field observations in terms of dominant wave periods of the tsunami-driven TIDs. This modeling study should be of great value to experimentalists, explaining why certain waves cannot be easily observed whilst others can be, thereby helping them interpret their TID observations.

References

Azeem, I., Vadas, S. L., Crowley, G., & Makela, J. J. (2017). Traveling ionospheric disturbances over the United States induced by gravity waves from the 2011 Tohoku tsunami and comparison with gravity wave dissipative theory. *Journal of Geophysical Research: Space Physics*, *122*, 3430–3447. https://doi.org/10.1002/2016JA023659

Crowley, G., Azeem, I., Reynolds, A., Duly, T. M., McBride, P., Winkler, C., & Hunton, D. (2016). Analysis of traveling ionospheric disturbances (TIDs) in GPS TEC launched by the 2011 Tohoku earthquake. *Radio Science*, *51*, 507–514. https://doi.org/10.1002/2015RS005907

Galvan, D. A., Komjathy, A., Hickey, M. P., Stephens, P., Snively, J., Tony Song, Y., … Mannucci, A. J. (2012). Ionospheric signatures of Tohoku-Oki tsunami of March 11, 2011: Model comparisons near the epicenter. *Radio Science*, *47*, RS4003. https://doi.org/10.1029/2012RS005023

Gossard, E. E., & Hooke, W. H. (1975). *Waves in the Atmosphere, Atmospheric Infrasound and Gravity Waves—Their generation and propagation* (pp. 456). New York: Elsevier Science.

Hedin, A. E. (1991). Extension of the MSIS thermosphere model into the middle and lower atmosphere. *Journal of Geophysical Research*, *96*, 1159–1172. https://doi.org/10.1029/90JA02125

Hedin, A. E., Fleming, E. L., Manson, A. H., Schmidlin, F. J., Avery, S. K., Clark, R. R., … Vincent, R. A. (1996). Empirical wind model for the upper, middle and lower atmosphere. *Journal of Atmospheric and Terrestrial Physics*, *58*, 1421–1447. https://doi.org/10.1016/0021-9169(95)00122-0

Hickey, M. P., & Yu, Y. (2005). A full-wave investigation of the use of a "cancellation factor" in gravity wave-OH airglow interaction studies. *Journal of Geophysical Research*, *110*, A01301. https://doi.org/10.1029/2003JA010372

Hickey, M. P., Schubert, G., & Walterscheid, R. L. (2009). Propagation of tsunami-driven gravity waves into the thermosphere and ionosphere. *Journal of Geophysical Research*, *114*, A08304. https://doi.org/10.1029/2009JA014105

Hickey, M. P., Schubert, G., & Walterscheid, R. L. (2010). Atmospheric airglow fluctuations due to a tsunami-driven gravity wave disturbance. *Journal of Geophysical Research*, *115*, A06308. https://doi.org/10.1029/2009JA014977

Hickey, M. P., Walterscheid, R. L., & Schubert, G. (2010). Wave mean flow interactions in the thermosphere induced by a major tsunami. *Journal of Geophysical Research*, *115*, A09309. https://doi.org/10.1029/2009JA014927

Holton, J. R. (2012). *An Introduction to Dynamic Meteorology* (5th ed.). San Diego, CA: Academic Press.

Komjathy, A., Galvan, D. A., Stephens, P., Butala, M., Akopian, V., Wilson, B., … Hickey, M. P. (2012). Detecting ionospheric TEC perturbations caused by natural hazards using a global network of GPS receivers: The Tohoku case study. *Earth, Planets and Space*, *64*, 1–8. https://doi.org/10.5047/eps.2012.08.003

Liu, J.-Y., Chen, C.-H., Lin, C.-H., Tsai, H.-F., Chen, C.-H., & Kamogawa, M. (2011). Ionospheric disturbances triggered by the 11 March 2011 *M*9.0 Tohoku earthquake. *Journal of Geophysical Research*, *116*, A06319. https://doi.org/10.1029/2011JA016761

Longuet-Higgins, M. S. (1962). Resonant interactions between two trains of gravity wave. *Journal of Fluid Mechanics*, *12*, 321–332. https://doi.org/10.1017/S0022112062000233

Makela, J. J., Lognonné, P., Hébert, H., Gehrels, T., Rolland, L., Allgeyer, S., … Lamouroux, J. (2011). Imaging and modeling the ionospheric airglow response over Hawaii to the tsunami generated by the Tohoku earthquake of 11 March 2011. *Geophysical Research Letters*, *38*, L00G02. https://doi.org/10.1029/2011GL047860

McComas, C. H., & Bretherton, F. P. (1977). Resonant interaction of oceanic internal waves. *Journal of Geophysical Research*, *83*, 1387–1412. https://doi.org/10.1029/JC082i009p01397

Occhipinti, G., Rolland, L., Lognonné, P., & Watada, S. (2013). From Sumatra 2004 to Tohoku-Oki 2011: The systematic GPS detection of the ionospheric signature induced by tsunamigenic earthquakes. *Journal of Geophysical Research: Space Physics*, *118*, 3626–3636. https://doi.org/10.1002/jgra.50322

Phillips, O. M. (1960). On the dynamics of unsteady gravity waves of finite amplitude. *Journal of Fluid Mechanics*, *9*, 193–217. https://doi.org/10.1017/S0022112060001043

Rolland, L., Lognonne, P., Astafyeva, E., Kherani, A., Kobayashi, N., Mann, M., & Munekane, H. (2011). The resonant response of the ionosphere imaged after the 2011 Tohoku-Oki earthquake. *Earth, Planets and Space*, *63*, 853–857. https://doi.org/10.5047/eps.2011.06.020

Smith, S. M., Martinis, C. R., Baumgardner, J., & Mendillo, M. (2015). All-sky imaging of transglobal thermospheric gravity waves generated by the March 2011 Tohoku earthquake. *Journal of Geophysical Research: Space Physics*, *120*, 10,992–10,999. https://doi.org/10.1002/2015JA021638

Vadas, S. L., Makela, J. J., Nicolls, M. J., & Milliff, R. F. (2015). Excitation of gravity waves by ocean surface wave packets: Upward propagation and reconstruction of the thermospheric gravity wave field. *Journal of Geophysical Research: Space Physics*, *120*, 9748–9780. https://doi.org/10.1002/2015JA021430

Walterscheid, R. L., & Schubert, G. (1990). Nonlinear evolution of an upward propagating gravity wave: Overturning, convection, transience and turbulence. *Journal of the Atmospheric Sciences*, *47*(1), 101–125. https://doi.org/10.1175/1520-0469(1990)047<0101:NEOAUP>2.0.CO;2

Yu, Y., Hickey, M. P., & Liu, Y. (2009). A numerical model characterizing internal gravity wave propagation into the upper atmosphere. *Advances in Space Research*, *44*(7), 836–846. https://doi.org/10.1016/j.asr.2009.05.014

Yu, Y., Yan, Z., & Hickey, M. P. (2015). Lower thermospheric response to atmospheric gravity waves induced by the 2011 Tohoku tsunami. *Journal of Geophysical Research: Space Physics*, *120*, 5062–5075. https://doi.org/10.1002/2015JA020986

Yu, Y., Wang, W., & Hickey, M. P. (2017). Ionospheric signatures of gravity waves produced by the 2004 Sumatra and 2011 Tohoku tsunamis: A modeling study. *Journal of Geophysical Research: Space Physics*, *122*, 1146–1162. https://doi.org/10.1002/2016JA023116